analytical chemistry

Article

pubs.acs.org/ac

Toward Three-Dimensional Chemical Imaging of Ternary Cu–Sn–Pb Alloys Using Femtosecond Laser Ablation/Ionization Mass Spectrometry

Valentine Grimaudo,[†] Pavel Moreno-García,[†] Andreas Riedo,[*,‡] Stefan Meyer,[‡] Marek Tulej,[‡] Maike B. Neuland,[‡] Miklós Mohos,[†] Christoph Gütz,[§] Siegfried R. Waldvogel,[§] Peter Wurz,[‡] and Peter Broekmann[†]

[†]Department of Chemistry and Biochemistry, University of Bern, Freiestrasse 3, 3012 Bern, Switzerland

[‡]Physics Institute, University of Bern, Sidlerstrasse 5, 3012 Bern, Switzerland

[§]Institute of Organic Chemistry, Johannes Gutenberg University Mainz, Duesbergweg 10-14, 55128 Mainz, Germany

Supporting Information

ABSTRACT: Femtosecond laser ablation/ionization mass spectrometry (LIMS) has been applied to probe the spatial element composition of three ternary Cu–Sn–Pb model bronze alloys (lead bronzes: CuSn10Pb10, CuSn7Pb15, and CuSn5Pb20), which were recently identified as high-performance cathode materials in the context of electro-organic synthesis (dehalogenation, deoxygenation) of pharmaceutically relevant building blocks. The quantitative and spatially resolved element analysis of such cathode materials will help in understanding the observed profound differences in their electrochemical reactivity and stability. For that purpose, we developed a measurement procedure using the LIMS technique which allows analyzing the element composition of these ternary alloys in all three spatial dimensions. Their chemical composition was determined spotwise, by ablating material from various surface locations on a 4 × 4 raster array (50 μm pitch distance, ablation crater diameter of ~20 μm). The element analyses show significant chemical inhomogeneities in all three ternary bronze alloys with profound local deviations from their nominal bulk compositions and indicate further differences in the nature and origin of these compositional inhomogeneities. In addition, the element analyses showed specific compositional correlations among the major elements (Cu, Sn, and Pb) in these alloys. On selected sample positions minor (Ni, Zn, Ag, and Sb) and trace elements (C, P, Fe, and As) were quantified. These results are in agreement with inductively coupled plasma collision/reaction interface mass spectrometry (ICP–CRI-MS) and laser ablation inductively coupled plasma mass spectrometry (LA-ICPMS) reference measurements, thus proving the LIMS depth profiling technique as a powerful alternative methodology to conventional quantification techniques with the advantage, however, of a highly localized measurement capability.

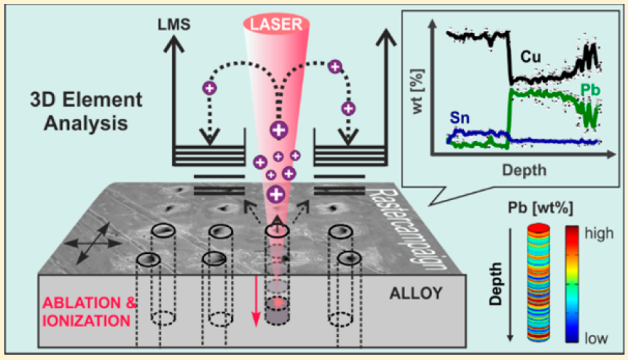

The electroreductive conversion of organic compounds, e.g., via dehalogenation or deoxygenation reactions, often requires harsh experimental conditions.[1,2] Typically, rather high overpotentials need to be applied to the cathode materials to obtain the desired product conversion to a significant extent.[3,4] The organic substrate molecule should be converted to the anionic species, which is quenched in the course of reaction by protons originating from the electrolyte. But, parasitic hydrogen evolution reaction (HER) is often superimposed on the primary electroreduction of interest limiting the faradaic efficiency (FE) of the desired reaction product when using aqueous electrolyte media. This is why materials such as Hg, Cd, or Pb are commonly used as cathode materials due to their high overpotentials with respect to the HER.[5,6] However, these cathode materials are not only per se environmentally unfriendly, but in addition, they suffer from corrosive degradation reactions, which often involve a release of the toxic cathode material (in particular Pb) in trace amounts into the electrolyte containing the desired reaction product. This cathodic corrosion can reach almost a stoichiometric degradation of the Pb metal indicating that intermediate and highly toxic organo-lead compounds might be formed.[7−10] Minimizing such corrosive cathode degradation effects is therefore essential for those electroreduction processes to become viable for industrial applications.[11,12] Various concepts have been discussed in literature. Cationic additives have already proven to stabilize in particular Pb cathodes against

Received: September 21, 2016
Accepted: January 2, 2017
Published: January 4, 2017

DOI: 10.1021/acs.analchem.6b03738
Anal. Chem. 2017, 89, 1632–1641

corrosion and to selectively suppress the HER.[13,14] Alternatively, improvement of the cathode material itself has been proposed. In this context, ternary Cu−Sn−Pb bronze alloys have been recently identified as promising candidates for cathode materials that indeed feature high overpotentials for the HER, high resistance against corrosion, and high FEs in dehalogenation reactions.[15] Many cathode materials have been tested in the electrosynthetic screening,[16] in particular ternary bronze-type alloys differing in the contents of the three major elements (Cu, Sn, and Pb). Electrode materials studied so far are CuSn10Pb10, CuSn7Pb15, and CuSn5Pb20. These three alloys are commercially available as lead bronzes exhibiting significantly enhanced mechanical strength compared to that of pure Pb.[17−19] Among them, it is in particular the CuSn7Pb15 alloy that showed a far superior performance over common pure Pb cathodes in context of dehalogenation reactions.[15] The chemical yield for the dehalogenation of the desired organic product and cathodic stability were outstanding, and the electrochemical process was superior to the conventional synthetic approaches.[20] Consequently, a technical upscaling with the CuSn7Pb15 alloy was performed.[21] Nonetheless, while these ternary Cu−Sn−Pb bronze alloys were already successfully tested, an atomic-scale understanding of the observed performance variations of those ternary bronze alloys is still missing as basis for a further and rational improvement of such cathode materials. This information is even more of interest knowing that the samples are not perfectly homogeneous and that the top surface, where the chemical reactions take place, is changing every time by processing the alloys. Therefore, a spatially resolved analysis of the element composition of these ternary alloys is required as a first step toward a better understanding of the observed variations in the cathode performance.

To date a variety of characterization techniques have been developed to address both chemical and material science questions for the chemical analysis of solid materials. However, these measurement apparatus are typically restricted to specific functions and differ from each other by their assets and drawbacks in terms of, e.g., detection sensitivity, quantification capabilities, spatial resolution (lateral and/or vertical), measurement acquisition velocity, etc. Transmission electron microscopy (TEM),[22] auger electron spectroscopy (AES),[23,24] and X-ray photoelectron spectroscopy (XPS)[24,25] are among others well-established analytical techniques with an impressive spatial resolution used for the imaging of structural compounds at submicrometer to few micrometers resolution and for the analysis of their element composition. Since the release of photoelectrons and Auger electrons originates from about a few monolayers depth, these techniques are limited to the analysis of the topmost surfaces[26] unless they are simultaneously combined to a material removal source. High spatial resolution often goes along with restricted measurement range capabilities. Atom probe tomography (APT) belongs to the forefront of high-resolution microscopy with unmatched chemical resolution at the atomic scale. APT, however, requires the fabrication of shaped specimens of certain geometry exhibiting an apex radius of ∼50 nm, which is nowadays accomplished by dual-beam focused ion beam (FIB)/secondary electron microscopy (SEM). This technique enables the three-dimensional atomic reconstruction of specimens, however, only for a small volume on the sample (nanometer scale). This approach is therefore not suitable for extensive 3D chemical investigation of larger objects. Moreover, compared to other imaging techniques, APT is an expensive, time-consuming, and destructive technique due to the site-specific preparation of the analyte and its rather slow acquisition system. Its routine application is additionally restricted to conductive materials, and sample breakage mechanism of the specimen induced by the strong electric fields is a recurrent issue.[25,27,28] The chemical characterization of bulk materials is these days typically carried out by methodologies based on spectrometric techniques, e.g., secondary ion mass spectrometry (SIMS),[29,30] glow discharge mass spectrometry (GD−MS),[31] and laser ablation inductively coupled plasma mass spectrometry (LA-ICPMS).[32,33] The lateral resolution of spectrometric systems is lower compared to spectroscopic measurements, e.g., AES and XPS, but benefits in turn from better detection sensitivities.[23] SIMS use is widespread in the semiconductor industry for surface contamination and depth profiling analysis due to its high achievable spatial resolution (lateral resolution for nanoSIMS <50 nm). However, high-resolution SIMS is restricted to the analysis of ultrathin layers (<micrometer depth), since depth profiling measurements of thicker layers require higher energy ion beams (>kiloelectronvolts) that cause sputtering-induced surface roughening and dramatically reduce the vertical resolution with increasing depth due to the intermixing of individual atomic layers.[30,34] GD−MS and LA-ICPMS are powerful analytical techniques with low matrix effects, fast analysis time, and low limits of detection (LOD). They suffer, however, from restricted spatial resolution (limited lateral resolution for GD−MS in the order of millimeters and limited depth resolution for LA-ICPMS of about 50 nm).[32]

To shed light on the spatial composition of the Cu−Sn−Pb alloys, we applied the femtosecond (fs) laser ablation/ionization mass spectrometry technique (LIMS). Our LIMS system developed at the University of Bern is a custom-made laser mass spectrometer originally designed for space exploration consisting of a miniature reflectron time-of-flight mass analyzer and bears the name LMS (laser mass spectrometer). This LIMS depth profiling technique was introduced by Grimaudo and co-workers in 2015 and already demonstrated nanometer depth resolution.[35−38] Recently, this depth resolution was pushed to the subnanometer level that even allowed for a structural analysis of impurities embedded at grain boundaries inside of a polycrystalline material with simultaneous chemical analysis.[35,36,38] Beside such high depth resolution it is in particular the quantitative nature of its mass spectrometric element analysis with a sensitivity of up to 10 ppb atomic fraction,[39] the high accuracy for isotope measurements,[40,41] and a high dynamic range ($\sim 10^8$)[39,40,42] that makes the LIMS technique a versatile alternative to well-established analytical techniques for depth profiling, such as LA-ICPMS,[32,33,43] GD−MS,[44] laser-induced breakdown spectroscopy (LIBS),[45] or SIMS.[29,46−49] Note, quantitative element analysis by means of SIMS is challenging[29,46−49] and, for example, is strongly affected by matrix effects.[50] This drawback particularly hampers the quantitative analysis of highly inhomogeneous alloy samples of unknown composition for which standards often are not available.

An important feature of the LMS setup is the femtosecond laser system that serves as source for the ablation and ionization of the sample material. The femtosecond laser ablation process guarantees a more uniform and spatially confined uptake of the sample material as compared to an ion bombardment process the SIMS technique is based on.[51,52] SIMS depth profiling of copper-rich phases particularly suffers from surface roughening

DOI: 10.1021/acs.analchem.6b03738
Anal. Chem. 2017, 89, 1632−1641

effects.[30,37] The use of a femtosecond laser ablation system further reduces undesired lattice heating effects (the femtosecond laser pulse duration is shorter than the material-specific thermal relaxation time), and it avoids interactions between the trailing part of the laser pulse and the ejected plume of material released from the sample surface. Hence, thermal effects and element fractionation are significantly reduced as compared to picosecond (ps) or nanosecond (ns) laser ablation systems. Therefore, element quantification becomes feasible without using any standards.[53−57]

In the present study, the experimental capabilities of our LMS setup were further developed by implementing an automated (programmed) raster mode and by improving the data analysis software. This study can be seen as a further step in our development of the LIMS technique toward chemical imaging of highly heterogeneous (inorganic) matter with lateral and vertical resolution in the micrometer and nanometer regimes, respectively.

MATERIALS AND METHODS

Sample. The three ternary Cu−Sn−Pb model alloy samples that were subjected to surface and bulk element analysis had nominal bulk compositions of CuSn10Pb10, CuSn7Pb15, and CuSn5Pb20 (denoted in the following as s1, s2, and s3, respectively). This notation refers to element fractions in weight percent (wt %), with 80 wt % Cu (matrix material), 10 wt % Sn, and 10 wt % Pb content in case of the CuSn10Pb10 alloy. According to the supplier, all three samples fulfill DIN (Deutsches Institut für Normung) norm 1716. The sample preparation and sample characterization by atomic force microscopy (AFM), X-ray diffraction (XRD), energy-dispersive X-ray spectroscopy (EDX), LA-ICPMS, and ICP−CRI-MS are described in the Supporting Information. Figure 1 exemplarily shows the surface morphology of sample s3 after LIMS depth profiling.

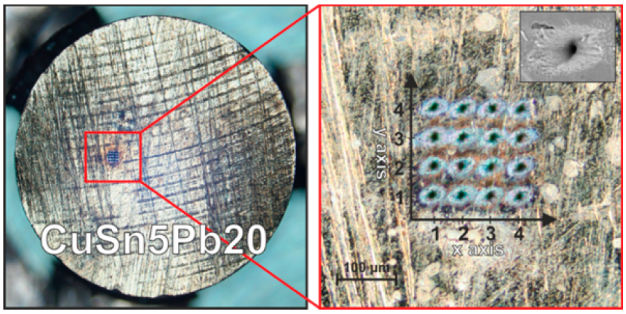

Figure 1. Representative optical micrographs showing the 4 × 4 array of LIMS craters on the ternary CuSn5Pb20 alloy. Clearly visible are deep grooves in the alloy material originating from the cutting and grinding treatment of the alloy sample (for details see the Supporting Information).

Laser Ablation/Ionization Mass Spectrometry. The LMS instrument[58] used for the element analysis of the Cu−Sn−Pb alloys consists of a miniature (160 mm × ø 60 mm) reflectron-type time-of-flight (R-TOF) mass analyzer. The ablation and ionization of the sample material was induced by a Ti-Sapphire laser system (CPA system, Clark-MXR Inc., U.S.A.) operating at a laser wavelength of 775 nm and generating ultrashort laser pulses with a pulse length of ∼190 fs at a laser pulse repetition rate of 1 kHz.[40] The principle of operation of the LMS instrument is described briefly in the Supporting Information. Detailed technical information and figures of merit of the LMS instrument are reported in previous publications.[39−41,59,60]

In Figure 2 a simplified scheme of the experiment setup is shown, including the femtosecond laser system, the mass analyzer, and the computer for data acquisition.

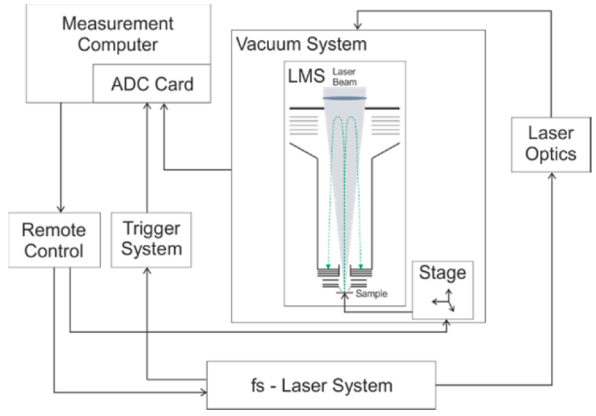

Figure 2. Scheme of the laser mass spectrometer (LMS) setup.

Measurement Procedure. Systematic LIMS chemical depth profiling has been carried out on each alloy sample in form of a 4 × 4 raster array with 50 μm pitch distance, covering a surface area of 150 × 150 μm^2 (corresponding to a lateral image resolution of 16 pixels). The image resolution is sufficiently high and the investigated area is sufficiently large to monitor both *surface* and *bulk* compositional inhomogeneities at the micrometer range. In principle, the lateral pixel resolution can further be increased (i) by reducing the pitch distance of the laser ablation craters which is limited only by their lateral diameter and (ii) by using software deconvolution procedures.[33] The optical micrographs in Figure 1 illustrate such a raster array of LIMS craters on sample s3. In total, 200 000 single laser shots were applied on each spot. Individual crater diameters have diameters in the range of ∼20 μm. To ensure stable ablation and ionization conditions a laser irradiance of ∼1.03 TW/cm^2 was applied. The inset in the SEM image of Figure 1 displays a typical LIMS crater, which shows much lower thermal alteration of the upper side walls (melting and resolidification) as compared to craters generated by nanosecond lasers. For data analysis, 200 single laser shot mass spectra were accumulated sequentially to one single cumulative mass spectrum on the acquisition cards (in total 1000 such cumulative mass spectra were recorded and saved for each spot on the host computer). In Figure 3 a representative cumulative mass spectrum is shown that was derived from sample s1. It shows isotope resolved mass peaks of singly charged Cu, Sn, and Pb representing the major elements of this ternary alloy with Cu having the highest element abundance followed by Sn and Pb.

The cumulative mass spectrum shown in Figure 3 further demonstrates the presence of cations carrying multiple charges (Cu^{2+}, Cu^{3+}, and S^{2+}). In addition, minor and trace elements are visible originating from either metallic contaminations in the alloy (e.g., Fe, Zn, and Ag), semimetallic components (e.g., Sb and As), or from nonmetallic impurities (e.g., P and S). The chemical mapping and the element correlation analysis (Figures 6 and 7) were calculated by considering only the major elements Cu, Pb, and Sn. The element abundance for Sn was

DOI: 10.1021/acs.analchem.6b03738
Anal. Chem. 2017, 89, 1632−1641

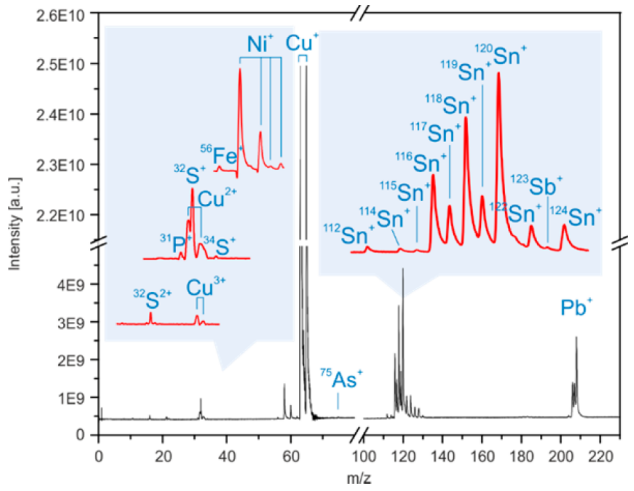

Figure 3. Representative cumulative mass spectrum derived from histogramming 200 single laser shot mass spectra that were acquired in sequence on sample s1 (CuSn10Pb10).

calculated considering only the ^{124}Sn isotope to avoid possible interferences with Sb.

The use of high laser irradiances could lead to undesired charging of the sample, e.g., surface charging, or Coulombic repulsion effects in the generated plasma plume, which might lower the mass resolution of our system. A custom-made data processing program was therefore developed that allows proper adjustment of the integration limits in each individual mass spectrum, which is particularly important for the quantification of Sn via its ^{124}Sn isotope. This approach led to more accurate signal integration even for those less resolved mass spectra that were actually affected by those charging effects. Mass spectra were not considered for the further analysis when the individual isotopes were not resolved. Element abundances were calculated by assuming terrestrial isotope ratios.[23] In contrast to Sn, a fixed integration window was applied for Cu and Pb, which considers all relevant isotopes of the respective element (Cu: ^{63}Cu and ^{65}Cu; Pb: ^{204}Pb, ^{206}Pb, ^{207}Pb, and ^{208}Pb). For the trace element analysis all detected mass peaks were considered, including multiply charged species and clusters. Especially for S and P considerable contributions of multiply charged species (2+, 3+, and 4+) to singly charged trace elements were observed (see Figure 3). Further information on the calculation of element abundances (in wt %) can be found in the Supporting Information. For the quantification of the element composition, a set of calibration factors with values ranging from 0.8 to 1.6, were derived and applied. For each alloy composition the ratio between the mean measured element abundance (derived from all conducted measurements on the sample) and the reported nominal bulk abundance of that corresponding element was calculated. The final applied calibration factor is the mean value of the individual ratios calculated for each alloy composition. A complete chemical analysis of each surface location is constructed from the element analysis of the 1000 cumulative mass spectra. For the 3D chemical mapping we restricted our analysis to Cu, Sn, and Pb, since these major elements are dominating the electrochemical activity of the alloys. Minor and trace elements are quantified only for selected sample locations to provide further insights into the mean impurity abundances.

To prove the accuracy of the LIMS measurements, the chemical compositions of the bulk alloys were independently determined by LA-ICPMS and ICP−CRI-MS measurements (for experimental details see the Supporting Information). The analysis results from all three techniques are summarized in Table 1.

After carrying out the LIMS chemical depth profiling, the samples were subjected to SEM, two-dimensional EDX (2D-EDX), AFM, and XRD analysis to gain more insights into their chemical composition and structure. A particular focus of this analysis was on the size distribution of segregated Pb particles inside the Cu−Sn matrix. The respective experimental procedures are described in the Supporting Information.

Cross-sectional SEM analysis of the LIMS craters was applied to determine the mean laser ablation rate of the LIMS depth profiling experiment. Appropriate cross sections of the LIMS craters were obtained by a mechanical polishing treatment of the samples using a diamond polishing slurry (MetaDi diamond suspension, for details see the Supporting Information). Our analysis revealed a total crater depth of about 38.4 ± 1.8 μm from which a mean ablation rate of about 38 nm/accumulated mass spectrum (200 single shot mass spectra) was determined for the applied laser fluence.

RESULTS AND DISCUSSION

Figure 4 shows the SEM and EDX analysis of polished cross sections of samples s1, s2, and s3. These structural and chemical analyses already demonstrate significant local fluctuations in the bulk composition and texture for all three alloy samples. A phase segregation of either lead-rich or even pure Pb clusters becomes obvious from the EDX mapping in Figure 4. This Pb segregation is characteristic for all three samples, but it is most pronounced in sample s2 (Figure 4, parts c and d). These Pb clusters are embedded into a Cu−Sn matrix where the Sn is more uniformly distributed inside the

Table 1. Composition Summary (wt %) of Samples s1−s3 Obtained by LMS, ICP−CRI-MS, and LA-ICPMS Techniques[a]

		DIN 1716	LMS	ICPMS	LA-ICPMS
CuSn10Pb10	Cu	78.0−82.0	78.61 ± 11.87	82.26 ± 4.13	76.99 ± 0.75
	Sn	9.0−11.0	9.94 ± 2.45	6.69 ± 0.79	10.91 ± 0.19
	Pb	8.0−11.0	12.25 ± 3.28	11.13 ± 0.63	8.56 ± 0.47
CuSn7Pb15	Cu	75.0−79.0	77.93 ± 11.77	75.55 ± 3.73	70.67 ± 1.03
	Sn	7.0−9.0	5.65 ± 1.39	6.56 ± 0.40	7.30 ± 0.06
	Pb	13.0−17.0	14.89 ± 3.99	19.45 ± 0.57	18.42 ± 1.04
CuSn5Pb20	Cu	69.0−76.0	76.37 ± 11.53	75.63 ± 3.39	74.94 ± 0.68
	Sn	4.0−6.0	5.99 ± 1.48	7.08 ± 0.73	6.92 ± 0.11
	Pb	18.0−23.0	15.63 ± 4.19	20.59 ± 1.25	16.59 ± 0.62

[a]The data from LIMS measurements was calibrated based on the nominal bulk composition (see main text for details).

DOI: 10.1021/acs.analchem.6b03738
Anal. Chem. 2017, 89, 1632−1641

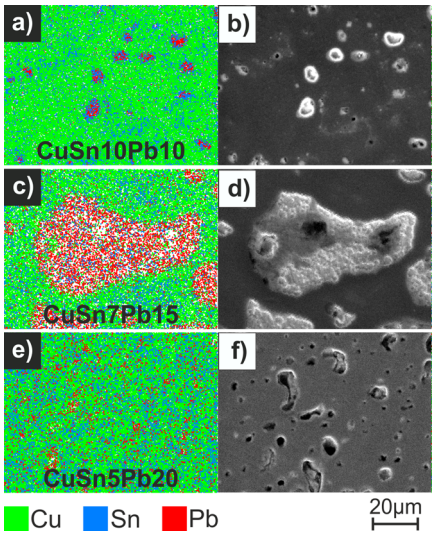

Figure 4. 2D-EDX element mapping (left) and corresponding SEM images (right) of the alloy samples s1 (a and b), s2 (c and d), and s3 (e and f) showing segregated lead-rich phases embedded into a binary Cu−Sn alloy matrix.

Cu. Segregated Pb clusters in sample s2 (highlighted in red in Figure 4c) reach diameters of >20 μm. In the SEM analysis, these Pb clusters are typically imaged with a higher (brighter) contrast (Figure 4, parts b and d). Note that these Pb clusters can in principle be removed from the topmost surface of the Cu−Sn matrixes in the course of the polishing treatment. A key parameter for the resulting surface finish of the alloy samples is the pressure applied to the alloy sample during the polishing treatment. This preparation effect is exemplarily demonstrated in Figure 4, parts e and f. Depressions seen in the respective SEM image (Figure 4f) correspond to those surface locations of sample s3 from where the segregated Pb clusters have been removed by the polishing. Due to this, a more uniform element distribution of Pb, Sn, and Cu is observed on the surface in the corresponding EDX mapping (Figure 4e).

These chemical and structural analyses are in full agreement with previous voltammetric experiments, which can now be rationalized by a superposition of cyclic voltammograms originating from the individual electrode materials (Cu−Sn and Pb).[15]

An immiscibility of Pb with the Cu−Sn matrix becomes further supported by our XRD data. Figure S-1 (see the Supporting Information) shows for all three lead bronze alloys an intense and sharp diffraction pattern that can be assigned to a nonalloyed (pure) lead phase (03-065-2873). The intensity of these lead-specific diffraction patterns proportionally increases along with the nominal lead concentration in these alloys in the sequence of $c_{Pb}(s1) < c_{Pb}(s2) < c_{Pb}(s3)$.

In contrast to the contribution of Pb to the X-ray diffractograms we observe for the respective Sn and Cu contributions peak broadening and in addition slight shifts of their diffraction peaks as compared to the respective pure Sn and Cu phases (01-071-7874: Cu0.932, Sn0.068). In addition, these experimental observations are indicative for Sn that is homogeneously distributed into the Cu, thus confirming our combined EDX mapping/SEM results (Figure 4).

Crucial for the interpretation of the LIMS depth profiling experiments (see below) is detailed information on the surface morphology and surface roughness of the alloy samples examined by this LIMS technique. For this purpose the SEM

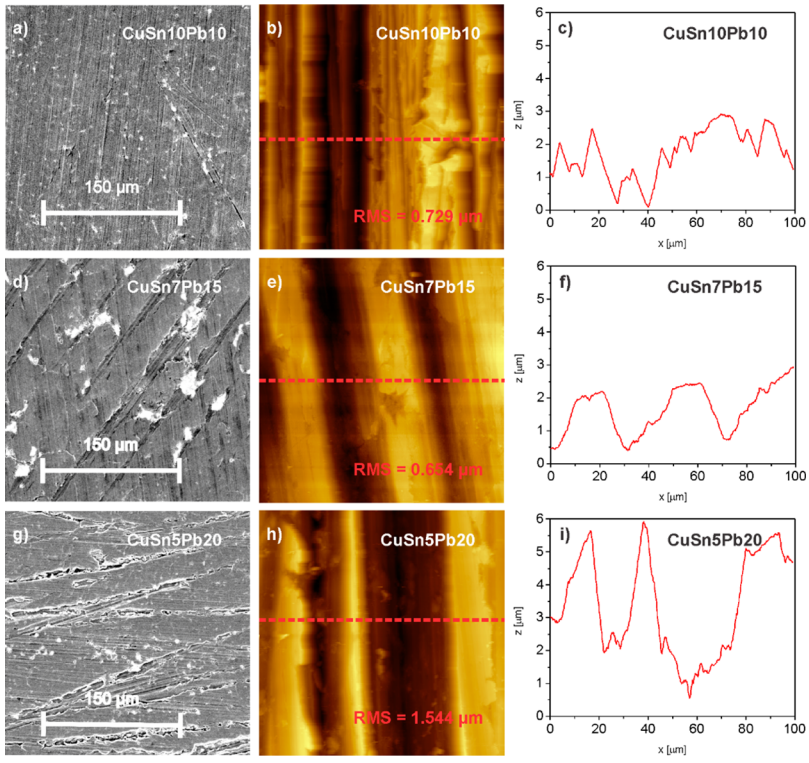

Figure 5. Surface roughness analysis of the as-received samples s1, s2, and s3: panels a, d, and g and panels b, e, and h display SEM and 100 × 100 μm^2 AFM images, respectively. Panels c, f, and i show topographical cross sections measured along the red dotted lines in the corresponding AFM images.

DOI: 10.1021/acs.analchem.6b03738
Anal. Chem. 2017, 89, 1632−1641

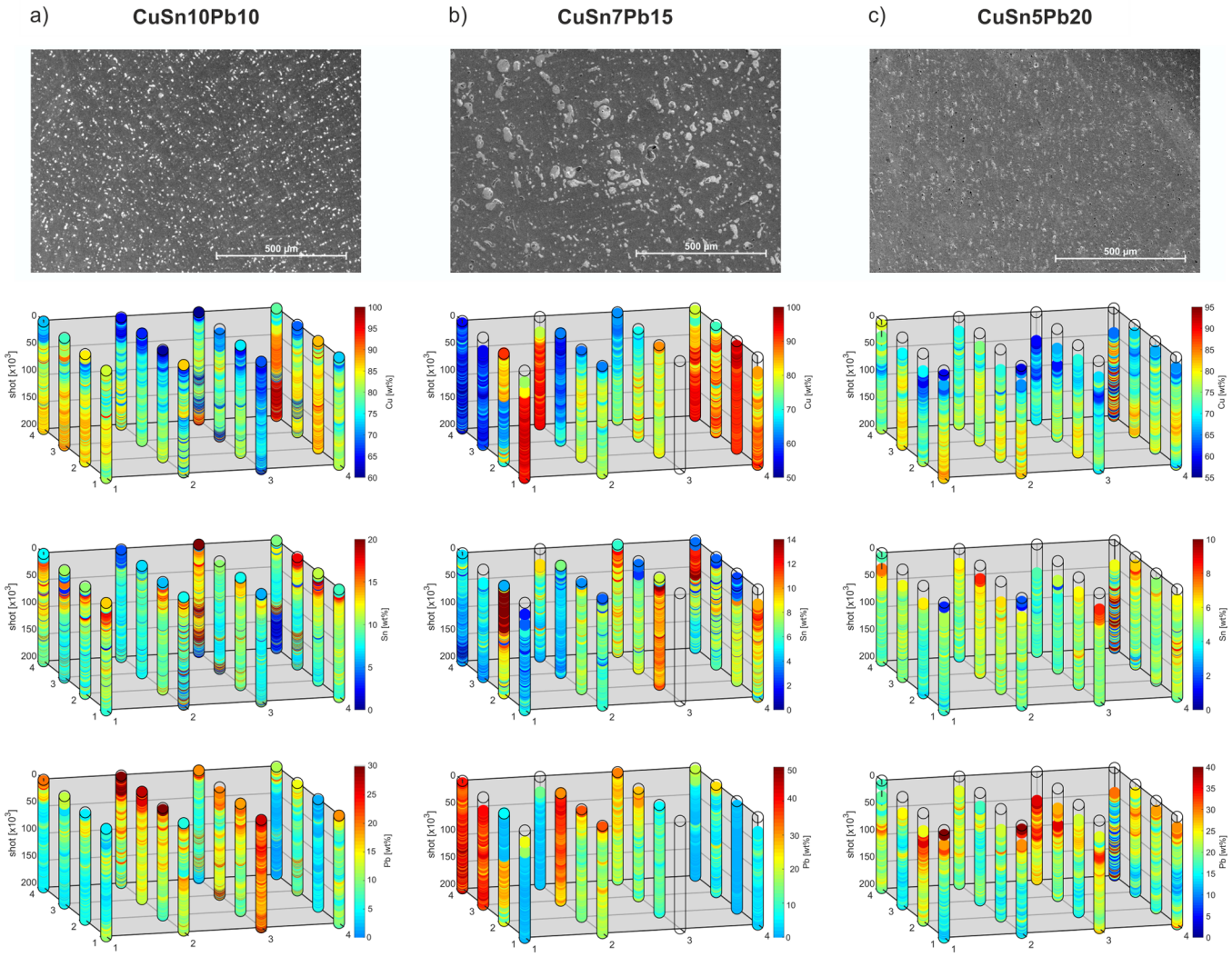

Figure 6. Cross-sectional SEM images (top row) and LIMS chemical mapping of the three ternary alloy samples on an array of 4 × 4 locations (bottom three rows), for the major elements Cu, Sn, and Pb: (a) sample s1, CuSn10Pb10; (b) sample s2, CuSn7Pb15; (c) sample s3, CuSn5Pb20.

surface analysis of the as-received alloy samples (see Figure 5, parts a, d, and g) was further complemented by an AFM inspection (Figure 5, parts b, e, and h). Besides the observed compositional inhomogeneities observed for the bulk of the alloy materials (e.g., Figure S-1), there are additional morphological features present at the surfaces of the as-received alloys in form of deep grooves and scratches (see Figures 1 and 5). These are typically aligned along a certain preferential direction on the sample surfaces (Figure 5). Grooves and scratches are the result of the initial cutting and grinding procedure of these alloy samples. The rms (root-mean-squared) roughness factors determined on the basis of the AFM imaging range from 0.729 μm (sample s1) to 1.544 μm (sample s3). It is the alloy sample s3 (Pb content of 20 wt %) that shows the highest surface roughness. It can be assumed that these specific surface features correlate with the different tribological characteristics of the lead bronze alloys. Sample s3 with highest Pb content can be considered as the softest material among the studied alloys.

From these considerations it can be concluded that the surface roughness of all samples studied is smaller at least by 1 order of magnitude than the depth of the respective LIMS craters, which is estimated to be 38.4 ± 1.8 μm (Figure 1).

Figure 6 displays the bulk morphology of the three alloy samples on a larger scale (topmost row) and the corresponding results of the LIMS depth profiling. For the representation of the horizontal and vertical element distribution we restrict ourselves to the major elements Cu, Sn, and Pb. For the sake of clarity, we plotted the abundance of each major element individually in 3D charts where the lateral spot position on the sample surface is indicated in the $x-y$ plane. The z-axis represents the crater depth in terms of number of applied laser shots. The element abundance in weight percent (wt %) is indicated by a specific color code that ranges from red (higher abundance than nominal bulk composition) to blue (lower abundance than nominal bulk composition). The color code was chosen in such way that the abundance of elements expected from the nominal bulk composition appears in green. As discussed above, only well-resolved mass spectra were considered for precise determination of element abundances. Nondisplayed data points in the 3D charts of Figure 6 appear as (partly) blank layers/rods. Poor mass resolution is occurring often for the uppermost part of s3. This phenomenon can be attributed to the higher surface roughness of this sample. The AFM measurements (Figure 5) reveal height corrugation in the order of ∼3−4 μm. These are believed to have a major effect on

DOI: 10.1021/acs.analchem.6b03738
Anal. Chem. 2017, 89, 1632−1641

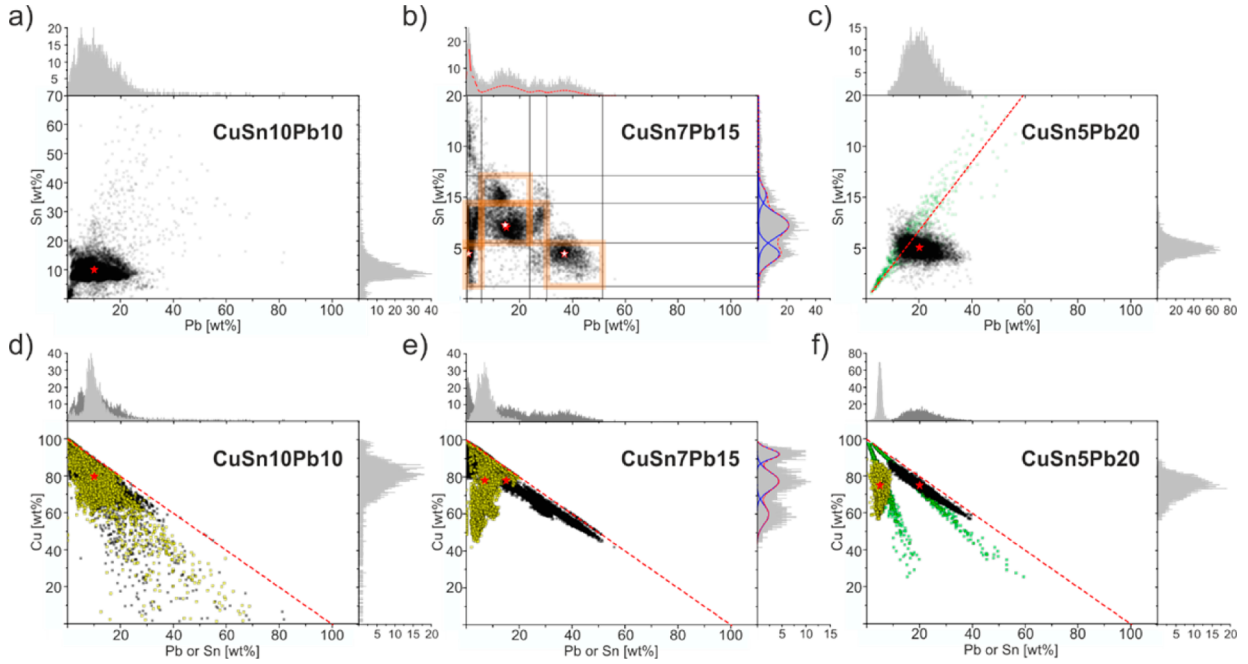

Figure 7. (a–c) 2D scatter plots and 1D histograms of the Sn/Pb abundance correlations; for s2 (panel b) the 1D histogram shows the contributions from the regimes identified in the 2D plot. The red asterisk indicates the nominal bulk composition, the open asterisk the composition of an individual regime. (d–f) 2D scatter plots and 1D histograms showing correlations of the Cu/Sn (yellow dots) and the Cu/Pb (black dots) abundances.

the crater evolution in the initial stage of the laser ablation process.

The chemical analyses presented in Figure 6 clearly show strong local deviations from the nominal bulk compositions. The observations confirm the compositional inhomogeneities that were already seen in EDX element maps (exemplarily shown in Figure 4), but now in all three spatial orientations of all three alloy model systems.

Sample s3 appears to be the most homogeneous one among the three alloys studied (Figure 6c). This finding is fully consistent with the EDX/SEM analysis showing much smaller segregated Pb clusters inside the Cu–Sn matrix, which are uniformly distributed inside the bulk material. However, in the near-surface regime there is an enrichment of Pb balanced by a deficiency in the Cu content. The Sn content, by contrast, seems to be unaffected by these local variations in the Cu and Pb concentrations along the *z*-direction. The Sn content is close to the expected nominal abundance of 5 wt %, both within the *x*–*y* plane and along the *z*-direction. The increased Pb concentration in the near-surface regime could be attributed to a sample preparation issue. The preferential enrichment of one element from the otherwise homogeneous sample could be assigned to a selective removal of one alloy component during the grinding treatment.

The most inhomogeneous sample, by contrast, is s2 (Figure 6b). Strong and anticorrelated abundance variations are observed in particular for Pb and Cu. This anticorrelation of the Pb and Cu contents is, however, not restricted to the near-surface regime as observed for s3 (Figure 6c) but extends to the entire investigated volume of the alloy sample. Therefore, these inhomogeneities are not solely related to a sample preparation issue but instead point to a pronounced phase separation into domains which are either copper-rich and almost lead-free [see spot (4,2) in Figure 6b showing locally Cu content of about 90 wt % or higher] or lead-rich and copper-deficient [see spot (1,4) in Figure 6b showing Pb content of up to 50 wt %]. A further indication for pronounced phase separation phenomena is the abrupt rise or decline of the Cu and Pb contents, respectively, as seen at the (1,2) spot of sample s2 (Figure 6b). Although less severe, also sample s1 shows compositional inhomogeneities in the entire investigated volume (Figure 6a) that again are dominated by the anticorrelated Cu and Pb abundances [compare respective spot (3,1) in Figure 6a]. A unique feature of sample s1 is, however, the presence of almost pure Cu phases [see bottom of the (4,4) spot in Figure 6a].

In Figure 7 specific abundance correlations among the Cu, Sn, and Pb contents including all information from the analyzed cumulative spectra of each of the three LIMS campaigns are shown (ideally, 16 000 cumulative spectra per sample). In panels a–c of Figure 7 the Sn contents were plotted versus the respective Pb contents on two-dimensional charts (2D scatter plots). In addition, the abundances of Sn and Pb were represented as separate 1D histograms. For the histogram construction we used a bin size in the wt % concentration of 0.01. For the sake of clarity we indicated the nominal composition of the respective alloy sample in the two-dimensional charts as red-filled asterisks.

A comparison reveals that the distribution of the Pb content is in all three cases (Figure 7a–c) significantly broader than the respective distribution of the Sn content. Among the samples, it is again sample s3 (Figure 7c) that appears to be the most homogeneous one. The maximum of the 1D histogram of the Sn content is found at 4.9 wt %, close to the nominal value of 5 wt %, whereas the maximum in the 1D histogram of Pb at 20.4 wt % is slightly above the nominal value of 20 wt %. A further characteristic of s3 (Figure 7c) is the absence of any domain that is largely lead-free. Indicated by the green dots in Figure 7c is a peculiarity in the Sn/Pb correlation plot, which originates from the (4,4) spot in Figure 6c and does not follow the general trend of s3. We interpret this singularity in Figure 6c as

DOI: 10.1021/acs.analchem.6b03738
Anal. Chem. 2017, 89, 1632–1641

a local inhomogeneity inside s3, which shows a linear correlation between the Sn and the Pb content as indicated by the red dotted line in Figure 7c. The high degree of inhomogeneity of sample s2 is apparent already in Figure 6b and becomes further corroborated by Figure 7b that shows multiple clearly discernible composition ratios for Pb and Sn contents, highlighted by the red open asterisk symbols. The broad and extended features in the 2D scatter plot indicate a Pb abundance that varies from almost 0 wt % to values of up to 51 wt %. Domains in s2 that are characterized by segregated lead-rich or even pure Pb phases embedded into the largely lead-free binary Cu−Sn alloy matrixes have already been imaged by the 2D-EDX mapping analysis (Figure 4). Domains of such binary Cu−Sn matrixes are represented in the 1D histogram of Pb (Figure 7b) by the pronounced maximum close to 0 wt % Pb, whereas the Sn content does not drop down to zero. Due to the lateral and depth resolution of the LMS instrument we observe Cu−Sn matrixes (largely lead free) in these 2D scatter plots. Compared to the spatially more extended Cu−Sn matrix the segregated lead-rich or even pure Pb phases are spatially much more confined. In this particular case, the spatial resolution of the LMS instrument in the surface plane is not sufficient to observe these pure or lead-rich phases without any contribution of the surrounding Cu−Sn matrix. It can therefore be assumed that the actual Pb content in those segregated Pb phases seen in the EDX element mapping (Figure 4) is above the highest abundances observed in the 2D scatter plot of Figure 7b. Furthermore, a weak correlation between the Pb and the Sn contents is visible. However, the identified domains represent Sn/Pb ratios for which an increased number of data points were observed. From the concentration distributions (1D histograms) it becomes clear that Sn and Pb are preferentially forming three, respectively four, distinct groups of element abundances. The peak maxima of the distribution profiles are assigned in the 2D plot with open asterisks. The highest concentration of data points is observed around the distribution peaks 7.2 wt % Sn and 14.5 wt % Pb, which are close to the expected nominal bulk values of 7 wt % Sn and 15 wt % Pb. The domain with the highest Pb content (peak maximum at 37 wt % Pb) shows the lowest Sn content (peak maximum at 4.4 wt %). Interestingly, a different Sn/Pb ratio with similar Sn content and extremely low Pb concentration (peak maximum at 0.7 wt %) is identified in the 2D correlation map.

In general, the 2D scatter plots in Figure 7a−c demonstrate that Sn and Pb abundances are weakly correlated to each other. Significant changes in the local Pb contents do not typically go along with accordingly drastic changes in the Sn content.

Compared to the Sn/Pb ratio the Pb/Cu correlation behaves differently. In Figure 7d−f we plotted the Cu versus the corresponding Pb and Sn contents (the Cu/Pb and Cu/Sn correlations are indicated by black and yellow symbols in Figure 7d−f, respectively). The most prominent feature visible in all three 2D plots is the strong (linear) anticorrelation between the Pb and Cu contents. Any increase of the Pb content leads to an equivalent drop in the Cu concentration (and vice versa), thus confirming the limited solubility of Pb in the Cu, or Cu−Sn, matrix. Such strong anticorrelation in the Pb/Cu contents is particularly pronounced for s2 and s3 (Figure 7, parts e and f) but more diffuse in case of s1 (Figure 7d).

In contrast to that, we observe only a minor change in the Sn content when the Cu content is decreased (yellow dots), in particular in case of s2 (Figure 7e) and s3 (Figure 7f) samples. This observation reflects the capability of Sn and Cu to form an alloy with only one phase. This conclusion is in agreement with the EDX mapping analysis (exemplarily presented in Figure 4c) showing a more uniform distribution of Sn in the Cu matrix.

An averaging of all our mass spectrometric measurements reveals the following bulk compositions of the three alloy samples studied (see Table 1): for s1 (nominal, Cu80Sn10Pb10) mean weight abundances of Cu 78.61 ± 11.87, Sn 9.94 ± 2.45, and Pb 12.25 ± 3.28 were measured. The 4 × 4 raster array of spots on sample s1 shows a deficit in the Cu content going along with an excess of Pb, whereas the Sn value is closer to the nominal value. For the s2 (nominal, Cu78Sn7Pb15) we determined a mean weight abundance of Cu 77.92 ± 11.77, Sn 5.65 ± 1.39, and Pb 14.89 ± 3.99. Finally for s3 (nominal, Cu75Sn5Pb20) we measured a mean weight abundance of Cu 76.37 ± 11.54, Sn 5.99 ± 1.48, and Pb 15.63 ± 4.19.

To stress the 3D chemical analysis capabilities of the LMS, Figure 8 shows a characteristic tin-rich grain embedded into the

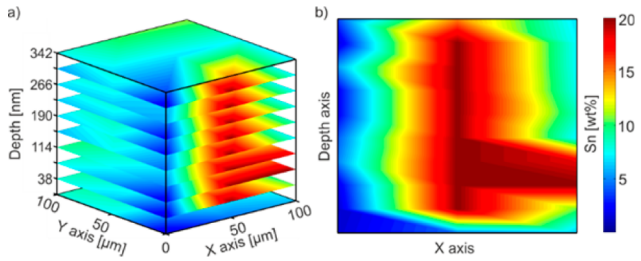

Figure 8. Tin-rich grain in the CuSn10Pb10 sample observed over 3 × 3 spots of the raster array and 10 consecutive depth layers (accumulated mass spectra): (a) slice plot illustrating the grain inside the Cu matrix; (b) *X*/depth interpolation of the 10 layers.

Cu matrix of s1. The grain was observed over 10 consecutive depth layers (accumulated mass spectra). Each layer was constructed from an interpolation of 3 × 3 lateral spot positions. On the basis of the calculated mean ablation rate we could estimate the height of the tin-rich grain to be about 350 nm, while the lateral dimension of the grain is in the micrometer range.

In order to verify the accuracy of the LMS results, independent ICP−CRI-MS and LA-ICPMS measurements were also carried out; the summary of the results is shown in Table 1. All three techniques yielded composition values that deviate only slightly from the nominal values. The table also includes the expected abundance ranges given by the DIN-norm.

Additionally, we analyzed minor and trace elements for selected spot positions; the results are summarized in Table S-1 in the Supporting Information. The mean values for minor and trace elements were derived on one sample position from 5 accumulated layers (5 × 200 shots) that showed sufficient mass resolution. The calibration factors for the trace elements were calculated from a model presented by Zhang et al., where the calibration factors for each element are expressed as a function of the plasma temperature T, the potential of first ionization IP, and the electron number density N_e.[61] From the mean calibration factors for Cu, Sn and Pb we derive an estimate of the theoretical parameters T and N_e, which are needed to calculate the calibration factors for minor and trace elements (Neuland et al.).[62] Since we calculate theoretical calibration factors based on a model, the listed abundances of the minor and trace elements in Table S-1 need to be considered as

DOI: 10.1021/acs.analchem.6b03738
Anal. Chem. 2017, 89, 1632−1641

semiquantitative. The calibration factors applied for these elements are within 0.8−1.1. The results for minor (Ni, Zn, Ag, and Sb) and trace elements (C, P, Fe, and As) were cross checked by LA-ICPMS and ICP−CRI-MS measurements as well. In accordance to the DIN-norm, in all three measurement techniques Ni and Zn turned to be the most abundant minor elements. In general, the results obtained from LIMS coincide well with the quantities reported from the reference measurements. Only Zn and Sb show lower abundances than expected, which could be explained by the interference of the trailing edge of the major isotopes with the isotopes of these elements. C and S could not be determined by LA-ICPMS due to high background noise and cluster interference.

CONCLUSION

We have employed LIMS technique to probe the chemical composition of three ternary Cu−Sn−Pb model alloy samples that are used as cathode materials in state-of-the-art electrosynthesis processes. The chemical mapping provides valuable information on the inhomogeneity of the alloy samples in three spatial dimensions. In particular, for s2, the measurements clearly demonstrate pronounced phase segregation with lead-rich domains that are embedded into binary Cu−Sn matrixes where the Sn is more uniformly distributed inside the Cu. It is the most inhomogeneous ternary Cu−Sn−Pb alloy of the three samples that has been identified in previous studies as the most active electrode material for electrosynthesis processes. For all three alloys studied a distinct anticorrelation in the Cu−Pb contents was observed confirming the limited solubility of Pb in Cu or copper-rich alloy matrixes. Alloy sample s3 was identified as the most homogeneous one. This alloy, however, exhibits gradients in the element composition along the surface normal with lead-enriched/copper-depleted phases in the near-surface regime. The latter effect could be assigned to sample preparation issues, which are most prominent in the lead-rich sample s3, the softest material among the three alloys studied.

The spatial chemical mapping of highly heterogeneous (electrode) materials will help to understand much better their particular reactivity in context of electrosynthetic reactions. Due to the inhomogeneity of the model alloys, the characteristics of the active area of the working surfaces vary in every electrosynthetic experiment. The enhanced electrochemical behavior of CuSn7Pb15 can be understood as an increased availability of micrometer-sized clusters of different chemical phases at the surface. In agreement with XRD measurements, 3D chemical imaging by LIMS revealed the existence of multiple Cu−Sn ratios and Pb segregation. However, the higher detection sensitivity of LIMS allowed for additional identification of specific Pb/Sn compositions that arise over the entire bulk. The electrosynthetic reactions are multistep sequences whereby the different phases may serve as the optimal cathodic material. Consequently, this approach of 3D element analysis may provide insights for a more rational electrode design in electro-organic synthesis.

These alloyed samples provide an optimal platform to demonstrate the capability of LIMS to perform localized quantitative 3D imaging experiments with high lateral and vertical resolution. The calibration procedure based on a statistically relevant number of applied measurements and the nominal composition of the material reproduced well the abundances from ICP−CRI-MS and LA-ICPMS reference measurements.

ASSOCIATED CONTENT

Supporting Information

The Supporting Information is available free of charge on the ACS Publications website at DOI: 10.1021/acs.analchem.6b03738.

Sample preparation and characterization, principle of operation of LMS, mass calibration and wt % calculations, minor and trace element analysis, and polishing procedure for crater cross sections (PDF)

AUTHOR INFORMATION

Corresponding Author

*E-mail: riedo@strw.leidenuniv.nl. Phone: +31 71 527 5815.

ORCID

Andreas Riedo: 0000-0001-9007-5791

Siegfried R. Waldvogel: 0000-0002-7949-9638

Author Contributions

The manuscript was written through contributions of all authors. All authors have given approval to the final version of the manuscript.

Notes

The authors declare no competing financial interest.

ACKNOWLEDGMENTS

We acknowledge the work from the technical staff of the Department of Chemistry and Biochemistry at the University of Bern, Switzerland. This work is supported by the Swiss National Science Foundation (SNSF). The German Federal Ministry of Education and Research is acknowledged for support of project MANGAN (FKZ 03S0506).

REFERENCES

(1) Grimshaw, J. *Electrochemical Reactions and Mechanisms in Organic Chemistry*, 1st ed.; Elsevier: New York, 2000.

(2) Peters, D. G. In *Organic Electrochemistry*; Lund, H., Hammerich, O., Eds.; Marcel Dekker: New York, 2001; pp 341−377.

(3) Hammerich, O.; Speiser, B. *Organic Electrochemistry*, 5th ed.; CRC Press: Boca Raton, FL, 2015.

(4) Yoshida, J.-i.; Kataoka, K.; Horcajada, R.; Nagaki, A. *Chem. Rev.* **2008**, *108*, 2265−2299.

(5) Grimshaw, J. *Electrochemical Reactions and Mechanisms in Organic Chemistry*; Elsevier: New York, 2000; pp 6−9.

(6) Liu, R.-S.; Zhang, L.; Sun, X.; Liu, H.; Zhang, J. *Electrochemical Technologies for Energy Storage and Conversion*; Wiley-VCH & Co. KGaA: Weinheim, Germany, 2012; Vols. *1 and 2*.

(7) Armstrong, R. D.; Bladen, K. L. *J. Appl. Electrochem.* **1977**, *7*, 345−353.

(8) Stohs, S. J.; Bagchi, D. *Free Radical Biol. Med.* **1995**, *18*, 321−336.

(9) Samarin, K. M.; Makarochkina, S. M.; Tomilov, A. P.; Zhitareva, L. V. *Elektrokhimiya* **1980**, *16*, 326−331.

(10) Fleischmann, M.; Pletcher, D.; Vance, C. J. *J. Electroanal. Chem. Interfacial Electrochem.* **1971**, *29*, 325−334.

(11) Kulisch, J.; Nieger, M.; Stecker, F.; Fischer, A.; Waldvogel, S. R. *Angew. Chem., Int. Ed.* **2011**, *50*, 5564−5567.

(12) Edinger, C.; Kulisch, J.; Waldvogel, S. R. *Beilstein J. Org. Chem.* **2015**, *11*, 294−301.

(13) Edinger, C.; Grimaudo, V.; Broekmann, P.; Waldvogel, S. R. *ChemElectroChem* **2014**, *1*, 1018−1022.

(14) Edinger, C.; Waldvogel, S. R. *Eur. J. Org. Chem.* **2014**, *2014*, 5144−5148.

(15) Gütz, C.; Selt, M.; Bänziger, M.; Bucher, C.; Römelt, C.; Hecken, N.; Gallou, F.; Galvão, T. R.; Waldvogel, S. R. *Chem. - Eur. J.* **2015**, *21*, 13878−13882.

DOI: 10.1021/acs.analchem.6b03738
Anal. Chem. 2017, 89, 1632−1641

(16) Gütz, C.; Klöckner, B.; Waldvogel, S. R. *Org. Process Res. Dev.* **2016**, *20*, 26−32.
(17) Aksoy, M.; Kuzucu, V.; Turhan, H. *J. Mater. Process. Technol.* **2002**, *124*, 113−119.
(18) Zohdy, K. M.; Sadawy, M. M.; Ghanem, M. *Mater. Chem. Phys.* **2014**, *147*, 878−883.
(19) Davis, J. R. *ASM Specialty Handbook: Copper and Copper Alloys*; ASM International: Materials Park, OH, 2001; pp 91−92.
(20) Baenziger, M.; Bucher, C. *Chim. Oggi Chem. Today* **2015**, *33*, 50−55.
(21) Gütz, C.; Bänziger, M.; Bucher, C.; Galvão, T. R.; Waldvogel, S. R. *Org. Process Res. Dev.* **2015**, *19*, 1428−1433.
(22) Rai, R. S.; Subramanian, S. *Prog. Cryst. Growth Charact. Mater.* **2009**, *55*, 63−97.
(23) Becker, J. S. *Inorganic Mass Spectrometry: Principles and Applications*; John Wiley & Sons Ltd.: Chichester, England, 2007.
(24) Reniers, F.; Tewell, C. *J. Electron Spectrosc. Relat. Phenom.* **2005**, *142*, 1−25.
(25) Escobar Galindo, R.; Gago, R.; Duday, D.; Palacio, C. *Anal. Bioanal. Chem.* **2010**, *396*, 2725−2740.
(26) Qian, G.; Li, Y.; Gerson, A. R. *Surf. Sci. Rep.* **2015**, *70*, 86−133.
(27) Cerezo, A.; Clifton, P. H.; Galtrey, M. J.; Humphreys, C. J.; Kelly, T. F.; Larson, D. J.; Lozano-Perez, S.; Marquis, E. A.; Oliver, R. A.; Sha, G.; Thompson, K.; Zandbergen, M.; Alvis, R. L. *Mater. Today* **2007**, *10*, 36−42.
(28) Bohannan, E. W.; Huang, L.-Y.; Miller, F. S.; Shumsky, M. G.; Switzer, J. A. *Langmuir* **1999**, *15*, 813−818.
(29) Vickerman, J. C.; Winograd, N. *Int. J. Mass Spectrom.* **2015**, *377*, 568−579.
(30) Hai, N. T. M.; Lechner, D.; Stricker, F.; Furrer, J.; Broekmann, P. *ChemElectroChem* **2015**, *2*, 664−671.
(31) Fernández, B.; Pereiro, R.; Sanz-Medel, A. *Anal. Chim. Acta* **2010**, *679*, 7−16.
(32) Gutiérrez-González, A.; González-Gago, C.; Pisonero, J.; Tibbetts, N.; Menéndez, A.; Vélez, M.; Bordel, N. *J. Anal. At. Spectrom.* **2015**, *30*, 191−197.
(33) Van Malderen, S. J. M.; van Elteren, J. T.; Vanhaecke, F. *Anal. Chem.* **2015**, *87*, 6125−6132.
(34) Hai, N. T. M.; Odermatt, J.; Grimaudo, V.; Krämer, K. W.; Fluegel, A.; Arnold, M.; Mayer, D.; Broekmann, P. *J. Phys. Chem. C* **2012**, *116*, 6913−6924.
(35) Grimaudo, V.; Moreno-García, P.; Riedo, A.; Neuland, M. B.; Tulej, M.; Broekmann, P.; Wurz, P. *Anal. Chem.* **2015**, *87*, 2037−2041.
(36) Riedo, A.; Grimaudo, V.; Moreno-Garcia, P.; Neuland, M. B.; Tulej, M.; Wurz, P.; Broekmann, P. *J. Anal. At. Spectrom.* **2015**, *30*, 2371−2374.
(37) Moreno-García, P.; Grimaudo, V.; Riedo, A.; Tulej, M.; Neuland, M. B.; Wurz, P.; Broekmann, P. *Electrochim. Acta* **2016**, *199*, 394−402.
(38) Moreno-García, P.; Grimaudo, V.; Riedo, A.; Tulej, M.; Wurz, P.; Broekmann, P. *Rapid Commun. Mass Spectrom.* **2016**, *30*, 1031−1036.
(39) Riedo, A.; Bieler, A.; Neuland, M.; Tulej, M.; Wurz, P. *J. Mass Spectrom.* **2013**, *48*, 1−15.
(40) Riedo, A.; Neuland, M.; Meyer, S.; Tulej, M.; Wurz, P. *J. Anal. At. Spectrom.* **2013**, *28*, 1256−1269.
(41) Riedo, A.; Meyer, S.; Heredia, B.; Neuland, M. B.; Bieler, A.; Tulej, M.; Leya, I.; Iakovleva, M.; Mezger, K.; Wurz, P. *Planet. Space Sci.* **2013**, *87*, 1−13.
(42) Riedo, A.; Tulej, M.; Rohner, U.; Wurz, P. *Rev. Sci. Instrum.* **2016**, Submitted for publication.
(43) Koch, J.; Günther, D. *Appl. Spectrosc.* **2011**, *65*, 155A−162A.
(44) Pisonero, J.; Bordel, N.; Gonzalez de Vega, C.; Fernandez, B.; Pereiro, R.; Sanz-Medel, A. *Anal. Bioanal. Chem.* **2013**, *405*, 5655−5662.
(45) Zorba, V.; Mao, X.; Russo, R. E. *Spectrochim. Acta, Part B* **2015**, *113*, 37−42.
(46) Werner, H. W. *Surf. Interface Anal.* **1980**, *2*, 56−74.
(47) Adriaens, A.; Van Vaeck, L.; Adams, F. *Mass Spectrom. Rev.* **1999**, *18*, 48−81.
(48) Patkin, A. J.; Morrison, G. H. *Anal. Chem.* **1982**, *54*, 2−5.
(49) Hofmann, S. *Rep. Prog. Phys.* **1998**, *61*, 827−888.
(50) Wurz, P.; Husinsky, W.; Betz, G. In *Symposium on Surface Science*, La Plagne, France, 1990; Launois, J. J., Mutaftschiev, B., Tempère, M. R., Eds.; Institute of Applied Physics: Wien, Austria, 1990; pp 181−185.
(51) Kelly, J. H.; Dowsett, M. G.; Augustus, P.; Beanland, R. *Appl. Surf. Sci.* **2003**, *203−204*, 260−263.
(52) Liu, R.; Ng, C. M.; Wee, A. T. S. *Appl. Surf. Sci.* **2003**, *203−204*, 256−259.
(53) Gao, Y.; Lin, Y.; Zhang, B.; Zou, D.; He, M.; Dong, B.; Hang, W.; Huang, B. *Anal. Chem.* **2013**, *85*, 4268−4272.
(54) Zhang, B.; He, M.; Hang, W.; Huang, B. *Anal. Chem.* **2013**, *85*, 4507−4511.
(55) Russo, R. E.; Mao, X.; Gonzalez, J. J.; Yoo, J. *Spectroscopy* **2013**, *28*, 24−39.
(56) Hergenroder, R.; Samek, O.; Hommes, V. *Mass Spectrom. Rev.* **2006**, *25*, 551−572.
(57) Zeng, X.; Mao, X. L.; Greif, R.; Russo, R. E. *Appl. Phys. A: Mater. Sci. Process.* **2005**, *80*, 237−241.
(58) Rohner, U.; Whitby, J. A.; Wurz, P. *Meas. Sci. Technol.* **2003**, *14*, 2159−2164.
(59) Neuland, M. B.; Meyer, S.; Mezger, K.; Riedo, A.; Tulej, M.; Wurz, P. *Planet. Space Sci.* **2014**, *101*, 196−209.
(60) Tulej, M.; Iakovleva, M.; Leya, I.; Wurz, P. *Anal. Bioanal. Chem.* **2011**, *399*, 2185−2200.
(61) Zhang, S.; Zhang, B.; Hang, W.; Huang, B. *Spectrochim. Acta, Part B* **2015**, *107*, 17−24.
(62) Neuland, M. B.; Grimaudo, V.; Mezger, K.; Moreno-García, P.; Riedo, A.; Tulej, M.; Wurz, P. *Meas. Sci. Technol.* **2016**, *27*, 035904.

DOI: 10.1021/acs.analchem.6b03738
Anal. Chem. 2017, 89, 1632−1641